



# New multi-fluid model of pool scrubbing in bubble rise region

Matic Kunšek<sup>a,b</sup>, Leon Cizelj<sup>a,b</sup>, Ivo Kljenak<sup>a,b,\*</sup>

<sup>a</sup> Jožef Stefan Institute, Jamova cesta 39, SI-1000 Ljubljana, Slovenia

<sup>b</sup> Faculty of Mathematics and Physics, University of Ljubljana, Jadranska ulica 19, SI-1000 Ljubljana, Slovenia

## ARTICLE INFO

### Keywords:

Aerosols  
Decontamination  
Pool scrubbing  
Multi-fluid

## ABSTRACT

A theoretical simulation model of solid particles behaviour inside a scrubbing pool was developed, with the purpose to evaluate the particles decontamination factor. A three-step approach to describe pool scrubbing on the local instantaneous scale, using Computational Fluid Dynamics, is proposed. A subgrid model for particle decontamination, based on simulation of particle flow within individual bubbles of different sizes, is introduced first. Experimental data from the literature were then used to first validate the used open-source numerical solver's gas-liquid flow part with the implemented drag model, and then to assess the results of pool scrubbing simulations using the implemented decontamination model.

## 1. Introduction

During a hypothetical severe accident in a light water reactor nuclear power plant, the fuel could melt and there is a possibility, that some radioactive material could be released within the containment. The purpose of pool scrubbing is to remove as much as possible radioactive substances (which can be in gaseous or particle form) from a mixture of condensable and non-condensable contaminated gases by filtering it through a liquid pool (in most cases water). The filtration efficiency of pool scrubbing can be expressed in terms of the Decontamination Factor (DF), which is defined as the ratio of the radioactive material mass entering to the mass leaving the pool. The present work considers pool scrubbing of particles.

To understand the mechanisms of pool scrubbing, phenomena at the local scale have to be considered. Because of the different behaviours of the gas-liquid-particles mixture during the process and different time and length scales of interaction between the phases, three successive regions in the vertical direction are usually defined (OECD/Nuclear Energy Agency, 1999; Herranz and Fontanet, 2013): injector region around the gas inlet, rise region, and surface region. The overall DF can be calculated as a product of DF for each region. Since gases enter the scrubbing pool as a jet that disperses into bubbles, the behaviour of the particle removal from the bubbles within the rise region is essential to understand pool scrubbing. Particles within bubbles move due to the centrifugal force (as they are being carried by the gas circulation, induced by the bubble motion), gravitational sedimentation, Brownian diffusion and eventually vapour condensation (if steam is present within

bubbles). An extensive description of bubble and particle phenomena in pool scrubbing may be found in the work of Powers (1997).

Up to now, most pool scrubbing theoretical simulations were performed with system codes for nuclear safety analyses: ASTEC, SPARC, BUSCA, MELCOR, COCOSYS and ECART (Abe et al., 2018; Dehbi et al., 2001; Herranz and Fontanet, 2013; Turni, 2016) that typically average physical quantities over large volumes. In the modelling of phenomena at the local scale, Wassel et al. (1985) have proposed a description of pool scrubbing, based on simplified one-dimensional basic equations and algebraic constitutive relations. Hozumi and Yoshizawa (1992) have modelled the motion of dust particles inside a single bubble in a jet bubbling reactor. Ghiaasiaan and Yao (1997) have proposed a model for deposition of aerosols in rising spherical bubbles. Ansari and Nimvari (2011) have modelled the circulation of gas within bubbles, but without particles.

As to the experimental investigations of phenomena within rising bubbles, one of the earliest documented works seems to be by Garner and Hammerton (1954), who have studied the gas internal circulation. Abe et al. (2018) have visualised the behaviour of particles in the gas. Fujiwara et al. (2019) have investigated the motion of particles within bubbles represented by oil drops. Much research on bubble motion and bubble swarm behaviour, which is important for theoretical simulation of pool scrubbing, was carried out without particles (Besagni et al., 2018; Dhotre and Smith, 2007; Rzehak et al., 2017; Simiano, 2005; Wardle and Weller, 2013).

It should also be noted that many experimental campaigns were carried out to measure how various parameters affect the DF. However,

\* Corresponding author at: Jožef Stefan Institute, Jamova Cesta 39, SI-1000 Ljubljana, Slovenia.

E-mail address: [Ivo.kljenak@ijs.si](mailto:Ivo.kljenak@ijs.si) (I. Kljenak).

<https://doi.org/10.1016/j.nucengdes.2022.111873>

Received 23 February 2021; Received in revised form 9 June 2022; Accepted 30 June 2022

Available online 13 July 2022

0029-5493/© 2022 The Authors. Published by Elsevier B.V. This is an open access article under the CC BY-NC-ND license (<http://creativecommons.org/licenses/by-nc-nd/4.0/>).

in most experiments, the overall DF was measured without insights into the two-phase flow behaviour of bubble columns (Dehbi et al., 2001; Kuhlman et al., 1986). Only few experiments were performed where both the DF and two-phase flow physical quantities were measured (such as by Turni, 2016).

The present work focuses on the rise region, where most of the particles migrate from the bubbles into the liquid. The gas decontamination was modelled using a multi-fluid approach with four phases: gaseous (bubbles), liquid, and two particle phases (within gas and within liquid). All phases were described in Eulerian frame. Simulations were performed using the open-source Computational Fluid Dynamics (CFD) code OpenFoam (Greenshields, 2015), with the solver reactingMultiphaseEulerFoam. As bubbles are much smaller than the numerical grid cells (hence the use of Eulerian frame), the transport of particles from the gas to the liquid phase was modelled using a proposed subgrid model that takes into account that the inner gas motion, caused by bubble rising, moves particles inside the bubbles due to interfacial drag. The particles first migrate towards the bubble surface and then out from the bubbles.

The main simplifying assumptions of the proposed modelling are spherical bubbles of uniform size (thus, no massive bubble coalescence), uniform particle size, and no particle conglomeration or agglomeration. The assumption of spherical bubbles is an approximation to irregular shaped bubbles that occur in the experiment, in which the overall deposition rate of particles should be similar, both qualitatively and quantitatively. In the presented simulations of some experiments, even some large bubbles (with equivalent diameter 1 cm) are modelled as spherical, although they were most probably (irregular) ellipsoidal or spherical-cap shaped. Also, neither Brownian diffusion nor diffusion of particles was modelled. The diffusion of the particles was not addressed, since as long as the particles are inside bubbles, the effect of air circulation within bubbles dominates the behaviour of particles. On the other hand, when particles reach the interface, they are considered to be in the liquid phase and their behaviour cannot affect the DF anymore.

The considered gas was air, so condensation was not considered. The prescribed particle densities and bubble diameters were based on data from the literature. The simulation results were analysed and the decontamination factor, which is the resulting measure of the scrubbing efficiency, was calculated and compared with experimental data. To the best of the authors' knowledge, this is the first attempt to simulate pool scrubbing experiments with a multi-fluid description, which represents a new step in the research of pool scrubbing.

## 2. Theoretical modelling of pool scrubbing

### 2.1. Model basics

In multi-fluid modelling (OECD/Nuclear Energy Agency, 1999; Frank et al., 2004), components (usually different phases) are treated as inter-penetrating continua, described by averaged conservation equations. The averaging process adds the phase fraction of each phase (defined as the probability that the considered phase is present at the observed location) into the equation set. The interphase momentum transfer is phase-fraction dependent and is determined from the forces acting on phases, comprising drag, lift and virtual mass forces. Problems arise from complex interactions between the considered fluids, which interact differently depending on the phase fraction of each fluid at the observed location.

In the present work, particle transport from bubbles to liquid is simulated as transfer, described by a subgrid model, from particles in the gas phase (particle phase 1) to particles in the liquid phase (particle phase 2). Due to the difference in the carrier phase, the particles' (inside or outside of bubbles) behaviour differ: the particles in the gas raise up with the gaseous phase and, in the end, leave the pool scrubbing tank, whereas the particles in the liquid stay in the tank. The difference between the two particle phases is only in the drag force correlations due to

their connection with the carrier phases (gas or liquid).

The location of particle phase 1 should be restricted to the domain region where gas is present. In numerical terms, this means, that the phase fraction of particle phase 1, whenever the gas phase fraction is low, is also lower for a few orders of magnitude. In the same way, the location of particle phase 2 should be restricted to the domain where liquid is present (in numerical terms, using the same principle as particle phase 1 and gas), and particle phase 1 and phase 2 cannot be present in the same domain region (again using the same principle). As phases ("phase" in the sense of the multi-fluid model) act on each other via drag, this is achieved by multiplying relevant drag forces by a small number: the drag between undesired phase pair becomes negligible and the equations become "semi-separated". The drag between the undesired phase pairs (air-particle phase 2, water-particle phase 1 and particle phase 1-particle phase 2) was thus multiplied by  $10^{-3}$  (value chosen arbitrarily). The four momentum equations in the solver can therefore become "semi-separated" to air-particle phase 1 and water-particle phase 2 parts. This corresponds to the idea of the subgrid model, where particle phase 1 does not interact with water and particle phase 2 does not interact with air.

In all simulations performed in the present paper, the material properties for air were set to perfect gas with molar mass of 28.9 g/mol and dynamic viscosity of  $1.84 \cdot 10^{-5}$  Pa·s, while the water was considered as a liquid with density of 1027 kg/m<sup>3</sup> and dynamic viscosity of  $2.82 \cdot 10^{-4}$  Pa·s.

In order to obtain a solution numerically, the computation domain has to be divided into computation cells. Because larger numbers of cells directly correspond to longer computation times, subgrid models are used in most simulations for objects that are much smaller than cell sizes. As these models need much lower numbers of cells to run, they are well-suited for use in industrial and nuclear installations. The current state of such modelling techniques is suitably described by Bonart (2012).

The used OpenFoam's multi-phase solver uses standard multi-phase balance equations for mass, momentum and energy for each phase, which are solved by the PIMPLE coupling algorithm (Greenshields, 2015).

Continuity equation:

$$\frac{\partial \alpha_i \rho_i}{\partial t} + \nabla \cdot (\alpha_i \rho_i \vec{v}_i) = \Gamma_i, \quad (1)$$

where  $\alpha_i$ ,  $\rho_i$ ,  $v_i$  and  $\Gamma_i$  denote respectively the phase fraction, density, velocity and interphase mass transfer of phase  $i$ .

Momentum equation:

$$\frac{\partial \alpha_i \rho_i \vec{v}_i}{\partial t} = -\nabla \cdot (\alpha_i \rho_i \vec{v}_i \vec{v}_i) - \alpha_i \nabla p_i + \nabla \cdot (\bar{\tau}_i + \tau_i^r) + \alpha_i \rho_i \vec{g} + \vec{M}_i, \quad (2)$$

where  $\nabla p_i$  is the pressure gradient of phase  $i$ ,  $\bar{\tau}_i$  is the average viscous stress of phase  $i$ ,  $\tau_i^r$  is the Reynolds stress of phase  $i$ ,  $\vec{g}$  is the gravity acceleration and  $\vec{M}_i$  is the average interphase momentum transfer for phase  $i$ .

In all simulations, the Schiller-Naumann (Wardle and Weller, 2013) drag force model was used:

$$\vec{M}_i = \sum_j^3 \frac{\rho_j \alpha_j C_D}{d_i} \frac{|\vec{v}_i - \vec{v}_j| \left( \vec{v}_i - \vec{v}_j \right)}{d_i}, \quad (3)$$

with:

$$C_D = \begin{cases} \frac{24(1 + 0.15Re^{0.683})}{Re}, & Re \leq 1000 \\ 0.44, & Re > 1000 \end{cases} \quad (4)$$

where  $\vec{M}_i$  is the interphase momentum transfer rate to phase  $i$  from

phase  $j$ ,  $\rho_j$  is the continuous phase density,  $C_D$  is the drag coefficient,  $d_i$  is the dispersed phase diameter and  $Re$  is the Reynolds number.

The procedure to develop a pool scrubbing simulation model consists of the following stages:

1. Two-phase simulation of particle deposition in a single spherical rising bubble
2. Gas-liquid flow solver verification
3. Multi-fluid pool scrubbing simulation

These stages are described below.

## 2.2. Modelling of particle deposition in spherical bubbles

For the first stage, simulations of particle deposition on wedge walls of single spherical rising bubbles were performed. Due to the gas motion within bubbles, particles move towards the bubble surface. A particle is considered to be removed when it is deposited on (that is, reaches) the bubble surface. As particles are considered to be located within the liquid from that moment, it is not necessary to consider the resistance of the interface to particles escaping deeper into the liquid to quantify the decontamination. A  $5^\circ$  wedge was chosen due to the rotational symmetry of the spherical bubble and to reduce computation time. From the decontamination of the wedge, the decontamination rate  $\frac{\partial m_{wedge}}{\partial t}$  was calculated as:

$$\frac{\partial m_{wedge}}{\partial t} = \Xi * m_{wedge}, \quad (5)$$

where  $m_{wedge}$  is the mass of particles in the bubble wedge,  $\frac{\partial m_{wedge}}{\partial t}$  is the particle mass flux from the wedge, and  $\Xi$  is some (unknown) decontamination function. Then, the decontamination rate for the entire bubble  $\dot{m}_{bubble}$  was calculated (Fig. 1, step a):

$$\dot{m}_{bubble} = \frac{\partial m_{bubble}}{\partial t} = \frac{2\pi}{\vartheta_{wedge}} \frac{\partial m_{wedge}}{\partial t}, \quad (6)$$

where  $\vartheta_{wedge}$  denotes the wedge angle.

After that, the decontamination rate in a cell  $\dot{m}_{cell}$  containing multiple bubbles was calculated as (Fig. 1, step b):

$$\dot{m}_{cell} = \frac{\partial m_{cell}}{\partial t} = \frac{S_{cell}}{S_{bubble}} \dot{m}_{bubble} = \frac{a_1 * V_{cell}}{\pi D_{Sm}^2} \dot{m}_{bubble}, \quad (7)$$

where  $S_{cell}$  is the interface surface in the computational cell,  $S_{bubble}$  is the mean bubble surface (in our case, all bubbles have the same surface size),  $a_1$  is the interfacial area density,  $V_{cell}$  is the cell volume and  $D_{Sm}$  is the Sauter mean diameter of bubbles.

If eqs. (5) to (7) are taken together, the particle decontamination rate for each cell can be calculated as:

$$\frac{\partial m_{cell}}{\partial t} = \frac{a_1 * V_{cell} * 2\pi}{\pi D_{Sm}^2 \vartheta_{wedge}} * \Xi * m_{wedge} \quad (8)$$

The process of the creation of the unknown decontamination function  $\Xi$  will be presented for spherical bubbles. The first selected diameter, which represents the bubble diameter, was 1.0 cm (later, cases with diameters 1.5 and 2.0 cm were also considered to determine the decontamination function for other bubble sizes). The numerical mesh in the bubble consisted of around 190,000 hexahedral computational cells. In this case, both phases were treated as fluids (particles as well to simplify calculations; namely, the difference in dispersed solid or dispersed liquid phase in the OpenFoam solver is only in the phase density change according to local parameters (Greenshields, 2015), which is, for this case, negligible.) The gas phase was set as continuous while the particle phase was set as dispersed. The boundary conditions (Fig. 2) for front and back plane were wedge symmetry. The wedge curvilinear wall was set as a rotational wall with a horizontal rotational axis (as rotation is due to bubble rising). The boundary condition at the rotational wall was set differently for each phase: for the gas phase, the wall was treated as no-slip with the prescribed rotation velocity which ensured that air does not leave the domain and rotates with the desired angular velocity; for the particle phase, the wall was set to free transition boundary condition, which ensured a free outflow of particles from the domain. The only connection between particle and gas phases was the interphase momentum transfer via drag force. The wedge wall rotating velocity was varied in 20 rad/s intervals from 20 rad/s to 400 rad/s. During simulations, the integral of particle mass in the domain was monitored in  $10^{-2}$  s intervals.

The initial conditions were both velocity fields set to zero and the particle volume fraction to  $5 * 10^{-7}$ ; the remaining part was air (which means, that eventual humidity within the bubbles was not considered).

The material ( $\text{SnO}_2$ ) and particle sizes were based on the data from the POSEIDON-II experiment (Dehbi et al., 2001; Dehbi et al., 2016).

The simulations were performed without considering gravity, as calculations show that particle settling is negligible. Namely, the ter-

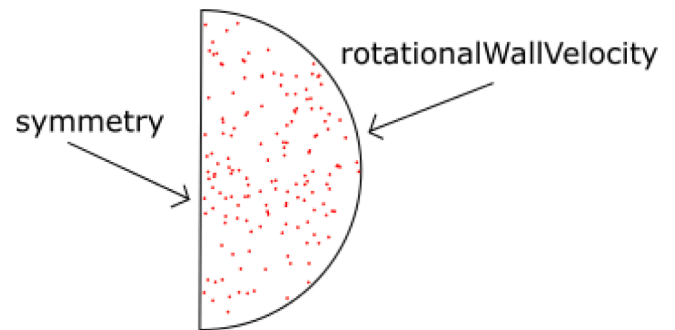


Fig. 2. Boundary conditions of wedge cases.

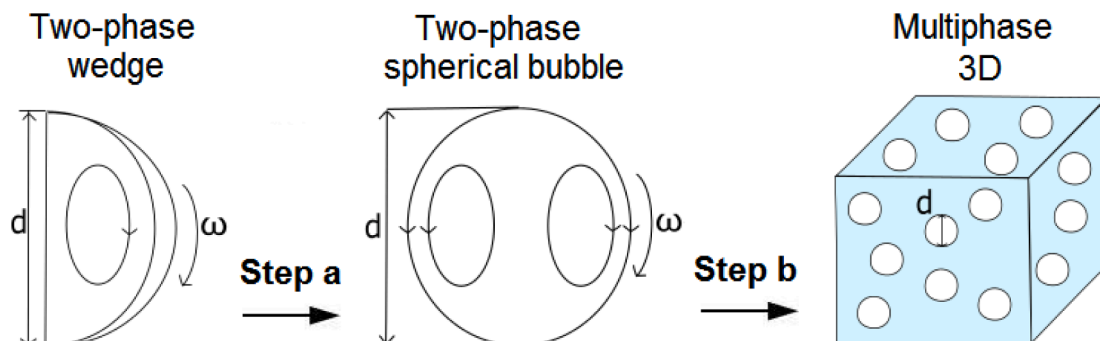


Fig. 1. Modelling stages.

minimal settling velocity  $\vec{v}_{set}$  can be calculated as:

$$\vec{v}_{set} = \vec{g}^* \tau_p, \quad (9)$$

where  $g$  is the gravity and  $\tau_p$  the particle relaxation time (Hinds, 1999), which can be calculated as:

$$\tau_p = \frac{\rho_p d_p^2 C_c}{18 \mu_f}, \quad (10)$$

where  $\rho_p$  is the particle density,  $d_p$  is the particle diameter,  $\mu_f$  is the carrier fluid dynamic viscosity and  $C_c$  is the slip correction factor that can be calculated as:

$$C_c = 1 + \frac{\lambda}{d_p} \left( 2.34 + 1.05 \exp\left(-0.39 \frac{d_p}{\lambda}\right) \right), \quad (11)$$

where  $\lambda$  is the mean free path of the carrier fluid (a commonly used value for air being 0.066  $\mu\text{m}$ ).

For particles used in the considered case, this leads to a relaxation time of 0.568  $\mu\text{s}$  and terminal settling velocity of 5.68  $\mu\text{m/s}$ , which is negligible in comparison to the velocities of air circulation inside bubbles (range from 0.1 m/s upwards).

### 2.3. Development of particle deposition model for multi-fluid modelling

After the simulation of particle deposition, the results were processed by the Matlab  $\text{\textcircled{R}}$  curve fitting application (MATLAB  $\text{\textcircled{R}}$ , 2018). In simulations, the phase mass cannot be monitored otherwise than through the phase volume fraction, so plots of particle volume fraction loss (deposition) rate over particle volume fraction were drawn. A polynomial fit was made for each result, using the following function:

$$\frac{\partial \alpha_{particle}}{\partial t} = A^* \alpha_{particle}^3 + B^* \alpha_{particle} = B^* \alpha_{particle}^* \left( 1 + \frac{A^*}{B^*} \alpha_{particle}^2 \right), \quad (12)$$

where  $A$  and  $B$  are constants. An illustrative example of results is shown in Fig. 3. The time derivative of particle volume fraction in the bubble and the normalized particle volume fraction are shown on the vertical and horizontal axes, respectively. Dots represent time steps of  $10^{-2}$  s when the integral volume of the particle phase was calculated. The first few values (red dots) are scraped due to the initialization of the rotational velocity field. An example of a fully developed air velocity field can be seen in Fig. 4. Overall, to determine particle deposition rate, 28 simulations were performed. The tested wall rotational velocities were varied in intervals of 20 rad/s. Seventeen (17) were done for bubble

diameter 1.0 cm from 40 rad/s to 400 rad/s, eight (8) for bubble diameter 1.5 cm from 20 rad/s to 260 rad/s and three (3) for bubble diameter 2.0 cm from 20 rad/s to 60 rad/s.

If the assumption is made that particles receive momentum only through the drag force, then the deposition rate of each bubble should be connected with the rotation velocity and the bubble volume. To illustrate – a higher rotation velocity means faster deposition. The same can also be stated for the bubble volume. This implies that the rotation velocity and the cube of the bubble diameter can also be factored out from the results. Thus, eq. (12) can be written as:

$$\frac{\partial \alpha_{particle}}{\partial t} = D^* \omega^* d_{bubble}^3 \alpha_{particle}^* \left( 1 + \frac{C^*}{D^*} \alpha_{particle}^2 \right) \quad (13)$$

where  $C$  and  $D$  are constants. This equation is then used as the wedge deposition function  $\Xi$ . The values of the constants  $C$  and  $D$  can be calculated as the slopes of the linear equations:

$$A = C^* \omega^* d_{bubble}^3 \quad (14)$$

$$B = D^* \omega^* d_{bubble}^3 \quad (15)$$

which leads to the values of  $C$  and  $D$  – 500.6  $\text{m}^{-3}$  and –0.002437  $\text{m}^{-3}$ , respectively.

To use eq. (13) in the multi-phase simulation, it has to be expressed with the fields that are used in that framework: the bubble rotation velocity  $\omega$  should be written in terms of the relative velocity between the gas and liquid phases:

$$\omega = \frac{|\vec{v}_r|}{r_{bubble}} = \frac{2 \left| \vec{v}_{air} - \vec{v}_{water} \right|}{d_{bubble}}, \quad (16)$$

where  $\vec{v}_r$  is the relative velocity between the phases,  $r_{bubble}$  is the bubble radius,  $\vec{v}_{air}$  is the air velocity and  $\vec{v}_{water}$  is the water velocity.

If eq. (13) is rewritten, one obtains:

$$\frac{\partial \alpha_{particle}}{\partial t} = D^* \frac{2 \left| \vec{v}_{air} - \vec{v}_{water} \right|}{d_{bubble}} d_{bubble}^3 \alpha_{particle}^* \left( 1 + \frac{C^*}{D^*} \alpha_{particle}^2 \right) \alpha_{particle} \quad (17)$$

Then, eqs. (13) and (17) are merged to create an equation usable in the multi-phase numerical simulation with the phases expressed in Eulerian frame for bubbles in computational cells. First, eq. (7) has to be rewritten from mass field to volumetric fractions, since the reactingMultiphaseEulerFoam solver uses volume fields and not mass fields:

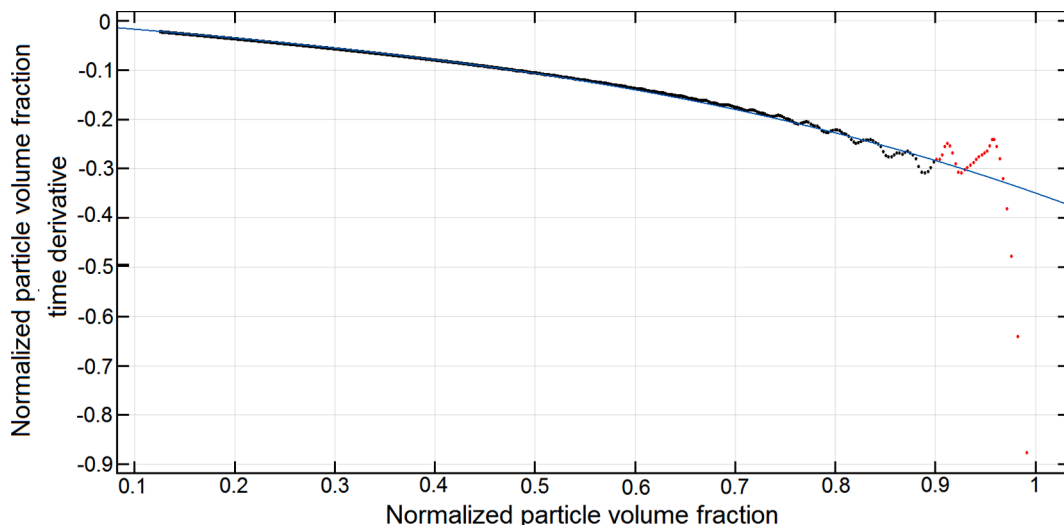


Fig. 3. Example of normalized deposition curve (bubble diameter: 1 cm; rotation velocity: 40 rad/s).

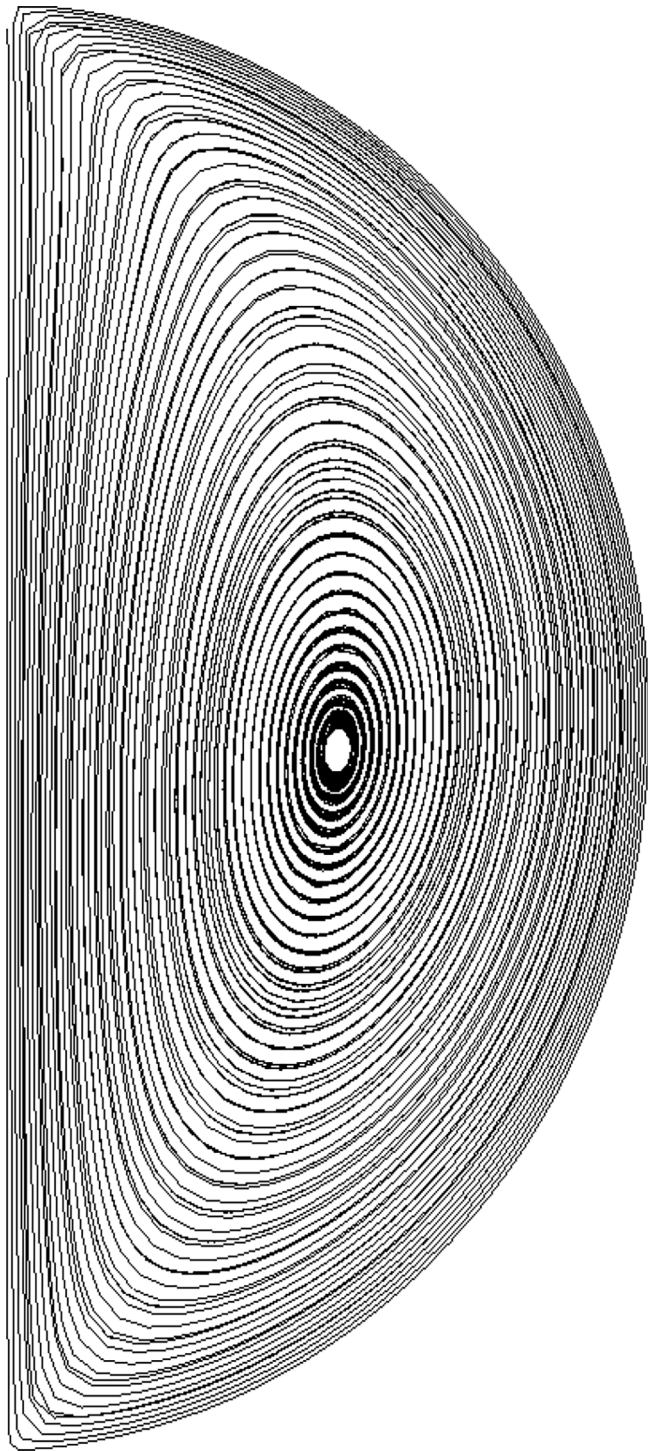


Fig. 4. Fully developed air velocity streamlines inside bubble wedge.

$$\frac{\partial \alpha_{particle}}{\partial t} = \frac{a_1 * V_{cell} * 2\pi}{\pi D_{Sm}^2 * \vartheta_{wedge}} * \Xi * \alpha_{particle}, \quad (18)$$

where  $a_1$  is the interfacial area density,  $V_{cell}$  is the cell volume,  $D_{Sm}$  is the mean bubble Sauter diameter,  $\vartheta_{wedge}$  is the used angle for the wedge case and  $\Xi$  is the wedge decontamination function. The merged equation reads as:

$$\frac{\partial \alpha_{particle}}{\partial t} = \frac{a_1 * V_{cell} * 2\pi}{\pi D_{Sm}^2 * \vartheta_{wedge}} * D^* \frac{2 \left| \vec{v}_{air} - \vec{v}_{water} \right|}{d_{bubble}} * d_{bubble}^3 * \left( 1 + \frac{C}{D} * \alpha_{particle}^2 \right) * \alpha_{particle} \quad (19)$$

Following the assumption that all bubbles are spherical, the substitution  $D_{Sm} = d_{bubble}$  can be made and the interfacial area density  $a_1$  can be expressed as (Ozaki et al., 2018):

$$a_1 = \frac{6 * \alpha_{air}}{d_{bubble}} \quad (20)$$

Equation (20) can be substituted into eq. (19), so that the equation to be added to the solver can be written as:

$$\frac{\partial \alpha_{particle}}{\partial t} = \frac{24 * \alpha_{air} * V_{cell} * D^*}{d_{bubble} * \vartheta_{wedge}} \left| \vec{v}_{air} - \vec{v}_{water} \right| * \left( 1 + \frac{C}{D} * \alpha_{particle}^2 \right) * \alpha_{particle} \quad (21)$$

Since eq. (21) will be added as a subgrid function, it will transfer the mass (volume) in the entire computation domain. To limit its influence only to the region where air flows in the form of bubbles (that is, in the rise region of pool scrubbing), the right-hand-side of eq. (21) should be multiplied by a weighting function. The most commonly used such function is the Heaviside step function. However, since it has a discontinuity in its own derivative, it can induce calculation errors. So, to get a smoother transition between the values of zero and one, the following function was used:

$$f_w(x) = \frac{1}{1 + \exp(C_{slope} * (x - C_{mid}))} \quad (22)$$

where  $\chi$  is the gas volume fraction,  $C_{mid}$  is the location in which  $f_w$  is 0.5 and  $C_{slope}$  indicates the inclination of the function at  $C_{mid}$ . The effect of variation of the constants can be seen in Fig. 5.

The chosen  $C_{mid}$  for the numerical simulations was 0.3 (transition from bubbly to slug flow in vertical pipes (Kunšek et al., 2016; Taitel et al., 1980)), while  $C_{slope}$  was chosen arbitrarily as 60. Thus, the right-hand-side of eq. (21) decreases from one to zero around the gas volume fraction 0.3, which was set as the upper limit of the rise region.

To test the sensitivity of the proposed model, some parameters of the simulation were varied. First, a mesh sensitivity study was performed. The tested meshes ranged from 23,500 cells to the original 190,000. The decontamination curves were plotted (Fig. 6) and fitted with the decontamination function. Given that the differences between the

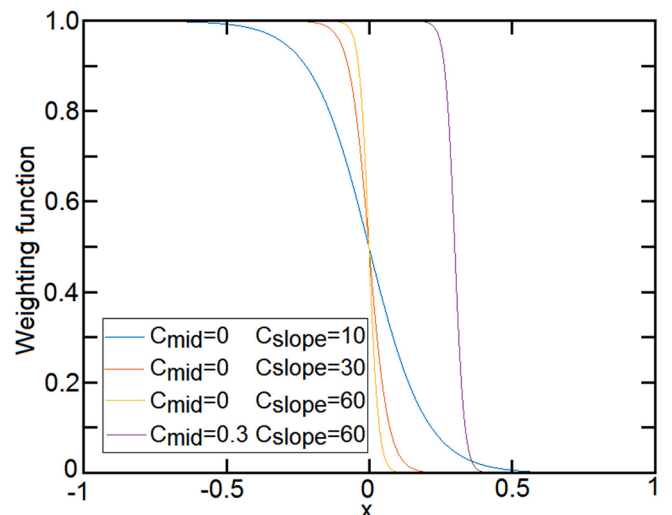


Fig. 5. Effect of variation of constants on weighting function.

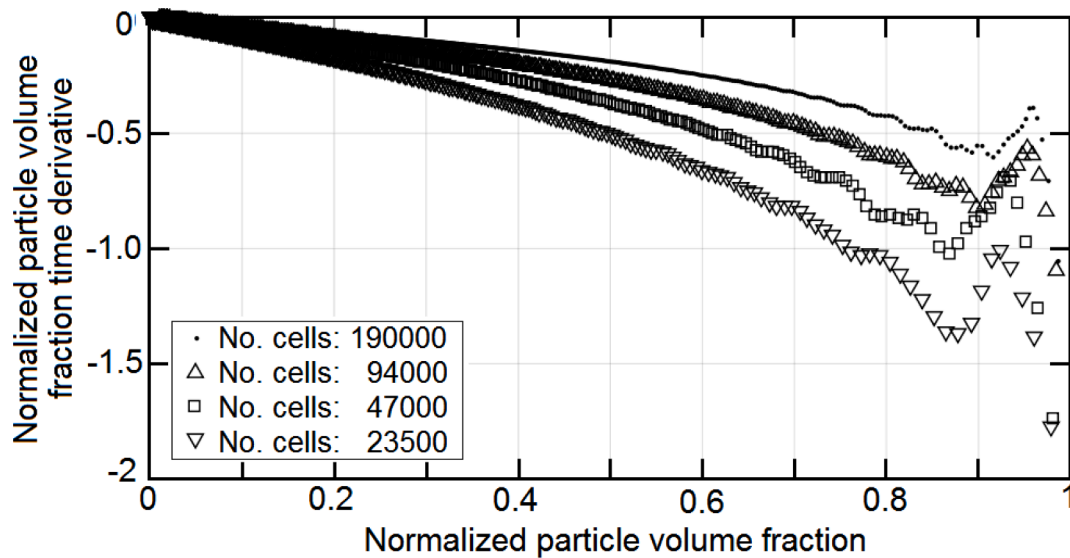


Fig. 6. Results of mesh sensitivity analysis on decontamination function.

results obtained with meshes from 23,500 to 190,000 cells gradually decrease, the authors considered that calculations with 190,000 cells may be considered sufficiently accurate.

After the confirmation that the used mesh is adequate, a study of the sensitivity on particle material parameters was performed. The selected parameters were particle size and particle material density. Simulations for particle deposition variations were performed for rotation velocities 60, 120 and 200 rad/s. For each rotation velocity, additional simulations were performed: one simulation for ten times larger particle diameter and three for varied particle density (0.1, 10 and 100 times the nominal particle density).

Again, the decontamination curves were fitted with the same function as before. The calculated constants were compared with the previously calculated ones and the relative change was calculated. This gave the possibility to quantify the difference of the particle deposition rate for single spherical bubbles with different particle sizes and material densities. From the results, it was seen that the effects of varying the particle sizes and the material density do not play a significant role in the proposed particle deposition model (all results are within 95% confidence bounds for a primary linear fit). The main reason for this is that the volumetric fraction of the particles is too small to influence the flow of air inside the bubble and therefore particles are, essentially but not completely, transported along the streamlines. Because the particle relaxation times are also small, the particles move similarly as the gas phase. Since the used OpenFoam solver does not take into account the diffusion of particles, which also contributes to the particle removal from bubbles, this numerical simulation still represents a simple model and therefore only an initial step to calculate the decontamination factor of pool scrubbing tanks.

### 3. Validation of gas–liquid flow modelling

#### 3.1. General description

As already stated, the second step was the gas–liquid flow part validation of the chosen OpenFoam solver (reactingMultiphaseEulerFoam). Namely, due to the complexity of pool scrubbing, the modelling of individual phenomena should be validated independently as much as possible, least the final calculated decontamination factor agrees well with the measured value only because of compensating errors.

The chosen experiments were LINX (Simiano, 2005) and SCRUPOS (Turni, 2016). The rationale for selecting these two experiments is that

the purpose of the LINX experiment was the investigation of bubble plumes in a pressure suppression pool (which may also be used for pool scrubbing), whereas the purpose of the SCRUPOS experiment was the investigation of pool scrubbing itself. In the LINX experiment, the flow in the inlet region is bubbly in the lower gas velocity ranges (up to 1.0 m/s), which corresponds to the flow at pool scrubbing conditions in the bubble rise region, while in the SCRUPOS experiments, the inlet is an actual high-velocity vertical jet that later disperses into bubbles. As the chosen physical model uses a drag correlation when the dispersed (gas) phase consists of bubbles, the calculated results should in principle agree better with the LINX experimental results than the SCRUPOS ones. Both experiments were simulated because in the SCRUPOS experiment, the decontamination factor was also calculated, which provides the unique option to simultaneously compare gas–liquid flow and decontamination results.

#### 3.2. LINX experiment simulation setup and model

The rise of air bubbles in a cylindrical tank (2.0 m diameter, 1.5 m liquid height) was simulated. The inlet (0.15 m diameter in the centre of the base of geometry) boundary condition was set to prescribed velocity. The prescribed bubble diameter was 2.5 mm, as in the work of Simiano (2005). The used drag correlation was the Schiller-Naumann one but multiplied with an additional coefficient  $K_{CD}$ , varied between 0.5 and 2 to better predict phase volume fraction and velocity profiles, as the correlation is valid for small spherical bubbles whereas bubbles in the experiment were reported to be wobbly.

The lift force, virtual mass and turbulent dispersion were modelled with constant parameters: coefficients were set to 0.1 for lift force, 0.5 for virtual mass and 0.05 for turbulent dispersion. The initial condition was stagnant water at temperature 300 K. The numerical mesh had around 120,000 cells, with a refinement around the inlet region.

The simulated cases were runs from the LINX test matrix 2 (Dhotre and Smith, 2007; Simiano, 2005) with air mass flow rates 0.14, 0.26, 0.55 and 1.10 kg/h.

#### 3.3. LINX experiment simulation results

The calculated values of air volume fraction and velocity were sampled in  $10^{-2}$  s intervals at various elevations above the inlet in 5 cm intervals. The results for each elevation were gathered and the mean value was calculated and compared with the experimental results.

Figs. 7 to 9 show comparisons of experimental and simulated profiles

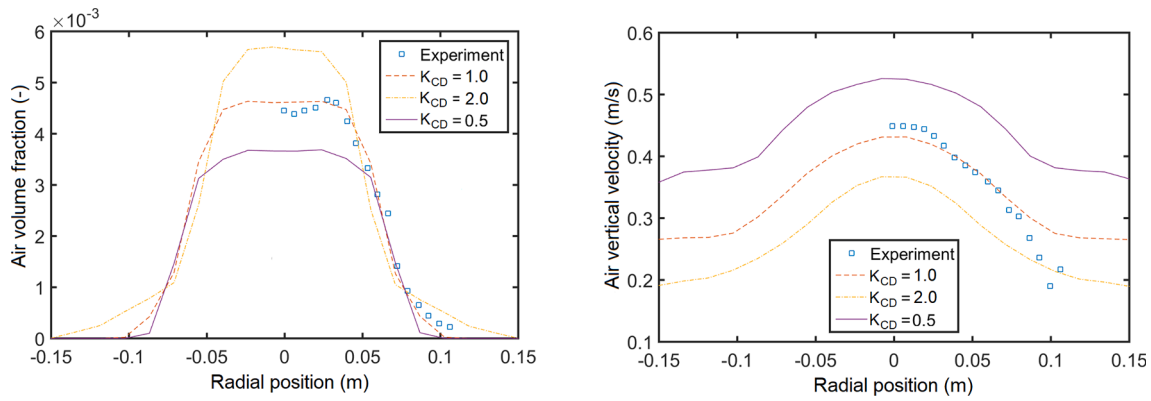


Fig. 7. LINX experiment (1.9 NL/min air vol. flow rate): air volume fraction and vertical velocity at 0.75 m elevation above inlet.

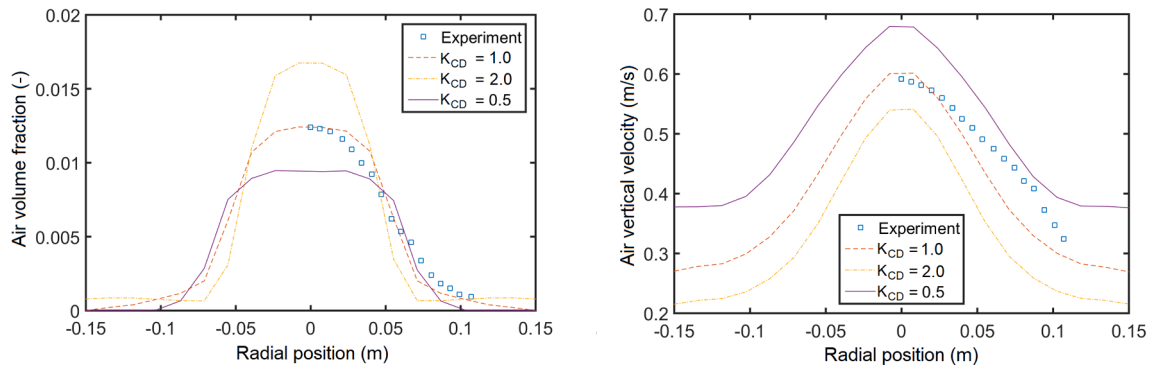


Fig. 8. LINX experiment (7.5 NL/min air vol. flow rate): air volume fraction and vertical velocity at 0.75 m elevation above inlet.

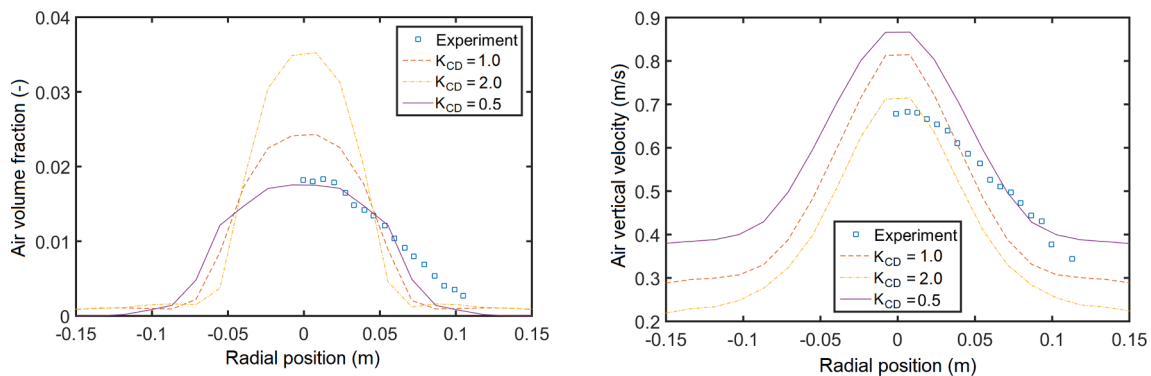


Fig. 9. LINX experiment (15 NL/min air vol. flow rate): air volume fraction and vertical velocity at 0.75 m elevation above inlet.

of air vertical velocity and air volume fraction at 0.75 m elevation above the inlet. The choice of these two physical quantities for the comparison is based on the premise that their influence is essential for the pool scrubbing process. For lower air vol. flow rates, the value 1.0 for  $K_{CD}$  seems to be the most adequate. For the highest air vol. flow rate, the best agreement for the air vertical velocity is obtained with  $K_{CD} = 2.0$ , whereas for air volume fraction, the best agreement is obtained for  $K_{CD} = 0.5$ . However, even for these two comparisons, simulations with  $K_{CD} = 1.0$  do not provide too high discrepancies, so that value seems to be the best compromise.

### 3.4. SCRUPOS experiment simulation setup and model

The rise of air bubbles, laden with particles, in a cuboid tank (1.0 m X 2.0 m base, 1.0 m liquid height) filled with water was simulated.

Although the inlet in the experimental facility has a diameter of 0.010 m, the inlet diameter in the model was prescribed as 0.10 m for numerical reasons, and this was compensated in the prescription of the inlet velocity to keep the same mass flow rate. As bubbles assume an intrinsic rise velocity depending on their size, the conditions in the rise region (that is, velocity and concentration of bubbles) should be sufficiently similar. The only major difference is that, in the simulation, the rise regime is assumed to start right above the inlet, whereas in the experiment, a jet injection regime occurred above the inlet before it evolved into the rise regime. Although this should in principle somewhat increase the decontamination factor, it is considered as part of the model simplifications.

In experiment and in simulations, the inlet is located in the centre of the base of geometry. The prescribed bubble diameter was 1.0 cm as described by Turni (2016). The numerical mesh had around 140,000

cells, with a refinement around the inlet to better describe its shape. Both particle phases were simulated as a dispersed liquid phase with a droplet diameter of 0.4 and 1  $\mu\text{m}$ , respectively.

The simulated experimental cases were performed with demineralized water. Experimental parameters are shown in Table 1, whereas the boundary conditions in the simulations are gathered in Table 2. The particles used were  $\text{SiO}_2$  with density  $2650 \text{ kg/m}^3$ . The inlet air velocity was calculated from the experimental mass flow rate and the inlet area in the simulation. The particle volume fraction was calculated as the ratio of air and particle volumetric flow rate. At the inlet, the velocities of particle 1 phase and air were set as equal. The inlet mass flows, for both phases, were regulated with the use of the volume fractions. In all cases,  $K_{\text{CD}}$  was set to 1.0. It should be noted that the experimental results of DF from the literature have specified a relative error within  $\pm 30\%$ .

### 3.5. SCRUPOS experiment gas–liquid flow simulation results

Figs. 10 and 11 show the experimental and simulated gas volume fraction and gas vertical velocity profiles for two different air mass flow rates, each time at three different elevations above the inlet. The process to acquire data for comparison was the same as in the LINX simulations.

Apart from the elevation closest to the inlet, where the simulated vertical velocity is lower than the experimental one for both air mass flow rates (which is probably due to the larger inlet area in the simulation), both simulated air volume fractions and vertical velocities are always higher than experimental values. However, as already seen in simulations of the LINX experiment, the prescription of  $K_{\text{CD}} = 0.5$  or  $2.0$  has the opposite effect on these two physical quantities. Thus, although one of the calculated variables could be closer to the experimental results by a suitable prescription of  $K_{\text{CD}}$ , that would increase the other quantity, making the discrepancy with experimental results even higher.

The fact that in SCRUPOS experiments, air is injected as a thin, high-velocity jet, and the drag model is not adequate for the later development of the flow, is the probable reason for the worse agreement of simulation and experimental results than in the LINX case.

According to the proposed decontamination model (eq. (21)), higher simulated air velocities than in the experiment should also cause, in the pool scrubbing part, higher decontamination factors than the experimental ones. Higher average volume fractions would also increase the decontamination factor. However, because of the high air volume fraction (higher than 0.3) close to the inlet, the onset of pool scrubbing could be shifted further downstream (because the bubble formation would begin later, thus at higher elevation) which could, in principle, decrease the decontamination factor.

Many other simulations of bubble plumes using multi-fluid modelling have also been described in the literature (for instance, recently by Besagni et al. (2018), Dhotre and Smith (2007), Rzehak et al. (2017) and Selma et al. (2010)). However, although better agreements between experimental and simulation results was sometimes obtained, to the best of the authors' knowledge, the LINX and SCRUPOS experiments, relevant for pool scrubbing, were never simulated with such an approach. Although the discrepancies between experimental and simulation results are in some particular cases significant, the general agreement was deemed acceptable to continue the application of the proposed model to

**Table 1**  
Parameters of simulated SCRUPOS experiments.

Case	Particle diameter [ $\mu\text{m}$ ]	Air mass flow rate [ $\text{kg/h}$ ]	Inlet particle concentration [ $\text{mg/m}^3$ ]	Experimental DF [-]	Relative exp. error [-]
T1	0.4	18	93.07	2	30
T2	0.4	24	52.5	2.62	30
T3	1	18	58.54	4.15	27
T4	1	24	16.75	2.77	27

**Table 2**  
Prescribed boundary conditions for simulation of SCRUPOS experiments.

Case	Inlet velocity [ $\text{m/s}$ ]	Particle 1 vol fraction [-]	Particle 1 diameter [ $\mu\text{m}$ ]
T1	0.640	$3.51 \cdot 10^{-8}$	0.4
T2	0.854	$1.96 \cdot 10^{-8}$	0.4
T3	0.640	$2.21 \cdot 10^{-8}$	1
T4	0.854	$6.32 \cdot 10^{-9}$	1

particle removal from the gas phase.

## 4. Simulations of pool scrubbing

The third stage of the presented work was the multi-phase pool scrubbing simulation. The subgrid model for particle transport from particle phase 1 to particle phase 2 was based on the results from the first stage, described in section 2.3. The decontamination factor was calculated and results were compared with SCRUPOS (Turmi, 2016) and EPRI (Kuhlman et al., 1986) experiments. For the SCRUPOS experiment, the same simulations were used as described in section 3.4.

To calculate the simulation decontamination factor, the inlet and outlet particle mass flow values were calculated by integrating particle 1 mass flows through the cells in both inlet and outlet patches in  $10^{-2} \text{ s}$  intervals. The decontamination factor was then calculated as the sum of all mass entering through the inlet divided by the sum of all mass exiting the domain through the outlet. Samples during the first 5 s were scrapped because of the time necessary for the first particles to reach the outlet of the computation domain (as the single bubble rise velocity is about 0.3 m/s for bubbles with 10 mm diameter, bubbles in 5 s move 1.5 m, which corresponds roughly to the depth of air inlet in the considered experiments).

### 4.1. SCRUPOS experiment decontamination factor simulation results

The results of the SCRUPOS experiment simulation of pool scrubbing, presented in Table 3, show that simulation decontamination factors are higher than experimental ones. Some explanations for the discrepancies can be proposed, based on the earlier discussion of results of the gas–liquid flow part. If we roughly quantify the discrepancies between experimental and simulation results, we may see that at the highest measuring point, the simulated air volume fraction is twice as high as the experimental one, and the simulated vertical air velocity is about 50% higher than the experimental one. From eq. (17), we may see that this may induce (if the water velocity does not change) a three-fold increase of the bubble decontamination factor. On the other hand, because of the much higher air volume fraction (thus longer jet region), bubble decontamination could start later and therefore reduce the bubble rise area and thus the decontamination factor. In addition, the side view of the gas volume fraction in the computation domain (Fig. 12) shows that if the average air volume fraction would be twice lower, the bubble rise region would be twice longer (because the bubbles form earlier). This means that simulations of SCRUPOS experiments would give about two to three times higher decontamination factors, which corresponds to the actual results from the simulations. Thus, the basis of the proposed model, that is, the subgrid model for particle transport from gas to liquid, seems adequate, and improvements are mostly necessary in the gas–liquid flow modeling part.

### 4.2. EPRI experiment setup

The EPRI experiment (Kuhlman et al., 1986; Ramsdale et al., 1992) (Fig. 13) was chosen because the flow regime in the inlet region is a horizontal jet. The jet then decays to bubbles over a large area, so that, in the vertical direction, the air initial velocity is close to 0 m/s. Therefore, it is expected that the simulation based on the proposed modelling will

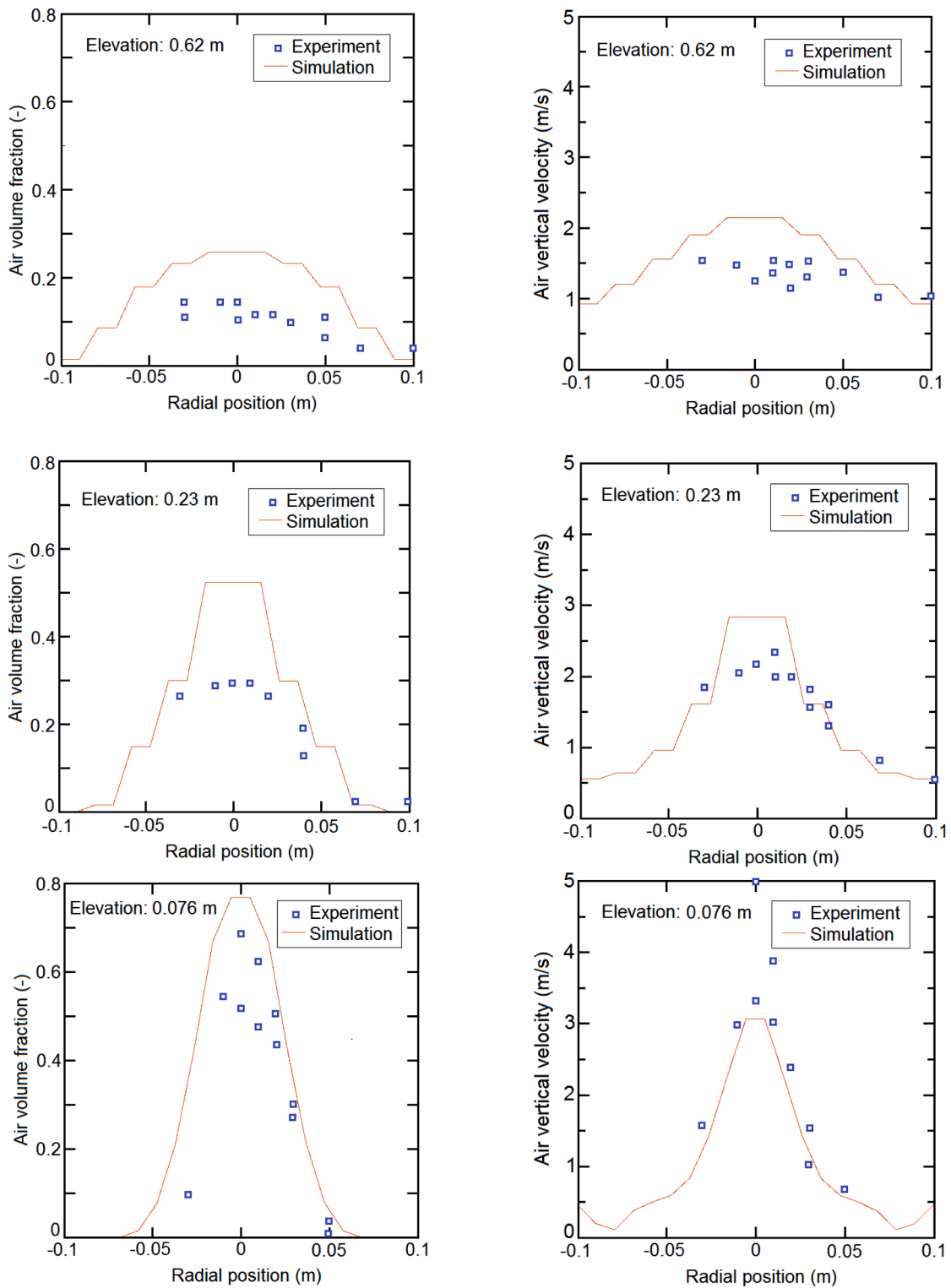


Fig. 10. SCRUPOS experiment (18 kg/h air mass flow rate): air volume fraction and vertical velocity.

give decontamination results that will be closer to the experimental decontamination factor than in the previously considered SCRUPOS experiment. The cases that are simulated correspond to the experimental campaign of near-saturated pool test conditions (Kuhlman et al., 1986): a mixture of gas and steam with particles are injected in a water pool with water temperature around 100 °C. Apparently, the goal of the experiments was to test how the condensation of steam enhances the decontamination factor. As, for the time being, condensation is not

included in the proposed model, the selected cases to simulate were those with no steam fraction (within the broader experimental campaign). In the experiment, CsI particles were used (density 4510 kg/m<sup>3</sup>). It should be noted that a relative experimental error for DF of about ± 20% is specified in the original reference.

The scrubbing pool has a diameter of 1.8 m and a height of 2.45 m. In the simulation, the part of the pool that is lower than the inlet was ignored to decrease the number of computational cells, since it may be

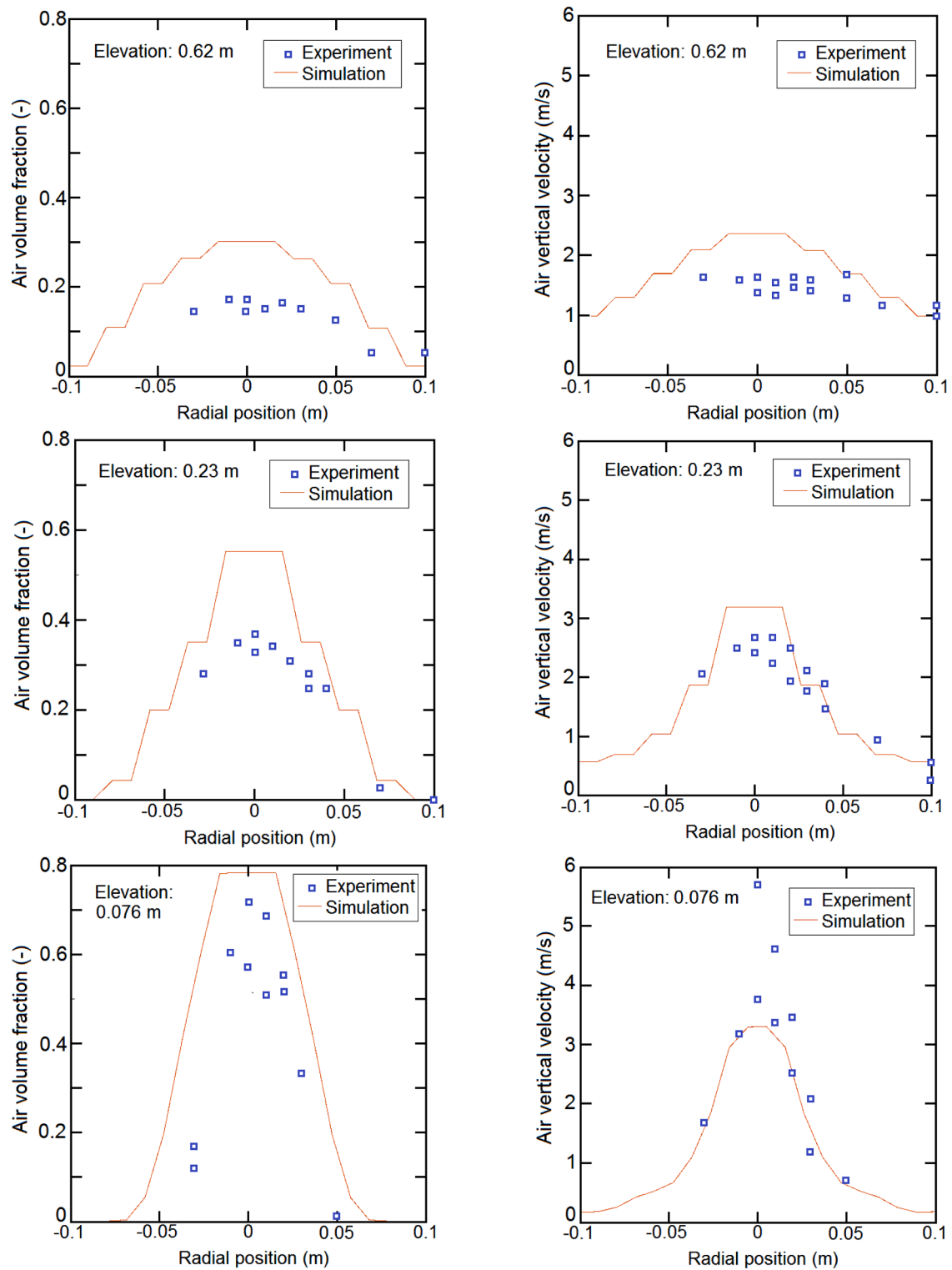


Fig. 11. SCRUPOS experiment (24 kg/h air mass flow rate): air volume fraction and vertical velocity.

**Table 3**  
Simulation results of SCRUPOS experiments.

Case	Particle diameter [μm]	Gas mass flow rate [kg/h]	Inlet particle concentration [mg/m <sup>3</sup> ]	Experimental DF [-]	Relative exp.error [%]	Simulation DF [-]
T1	0.4	18	93.07	2	20	6.15
T2	0.4	24	52.5	2.62	30	4.43
T3	1	18	58.54	4.15	27	6.33
T4	1	24	16.75	2.77	27	4.70

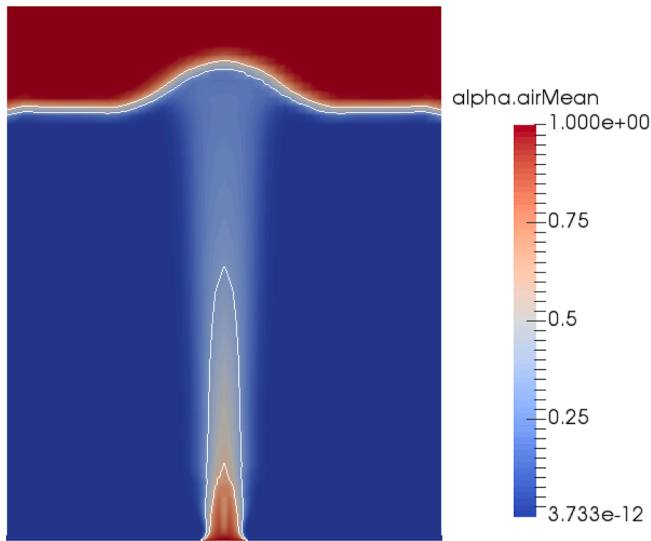


Fig. 12. SCRUPOS experiment: side view of air volume fraction for simulation of case T2 (white lines show 0.3 and 0.6 air volume fraction contours).

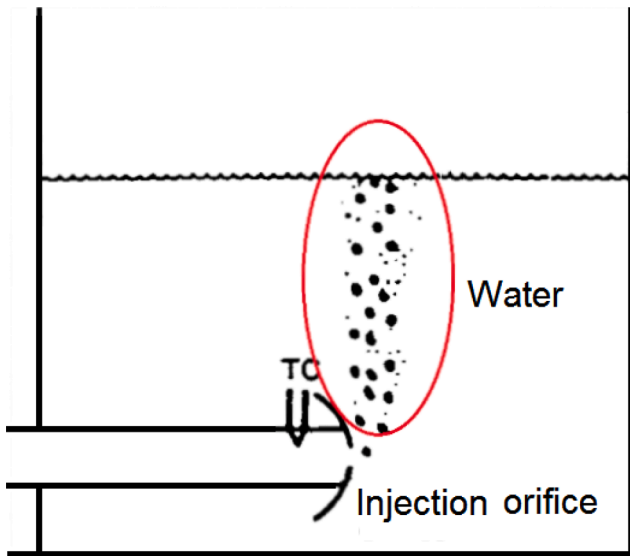


Fig. 13. Schematic of EPRI experiments injection (as illustrated by Escudero Berzal et al., 1995; the red ellipse shows the part of the experiment considered in the simulation).

assumed that it has little impact. As the actual inlet part of the experiment was not simulated, in the simulation, the initial gas velocity is vertical, the inlet, positioned in the centre of the base of the volume, (with diameter set to 5.0 cm) is also vertical and has no relation to the diameter of the injection tube in the experiment. The injector submergence was set to 1.65 m of depth as in the experiment (Kuhlman et al., 1986). The prescribed bubble diameter was 1.0 cm, chosen arbitrarily. The numerical grid consisted of about 100,000 cells.

At the inlet, the velocities of particle phase 1 and air were set to equal values. The inlet mass flows, for both phases, were regulated with the use of the volume fractions. The inlet conditions that vary between the cases are presented in Table 4.

To test the influence of inlet dimension variation on the results, multiple meshes were developed, where the inlet radius dimension was varied within  $\pm 0.5$  cm. To test the influence of the drag coefficient variation on the results, the Schiller-Naumann drag model was multiplied with coefficients  $K_{CD}$  ranging from 0.5 to 1.5 for the selected case.

Table 4

EPRI experiment boundary conditions and experimental decontamination factor.

Case	Gas inlet velocity [m/s]	Particle volume fraction [-]	Experiment DF [-]
E1	0.576	$6.94 \cdot 10^{-8}$	$7.7 \pm 1.3$
E2	0.601	$7.65 \cdot 10^{-8}$	$8.6 \pm 1.3$
E3	0.581	$4.91 \cdot 10^{-8}$	$5.0 \pm 0.4$
E4	0.576	$1.17 \cdot 10^{-7}$	$12 \pm 2.2$
E5	0.576	$1.36 \cdot 10^{-7}$	$6.2 \pm 0.6$

### 4.3. EPRI experiment simulation results

As an illustration, results of the E1 case parameter variations are shown in Fig. 14 (the other cases behave similarly). It can be seen that decontamination factors with the same drag multiplication constant ( $K_{CD}$ ) are similar. An interesting observation is that the results obtained with  $K_{CD} = 1.5$  are similar to those obtained with the plain Schiller-Naumann model.

The results of the runs for the simulations with the pure (no added multiplication factor) Schiller-Naumann drag model are shown in Fig. 15. The results that agree best with the experiment were achieved with the largest inlet area, probably due to lower inlet velocities and thus more in accordance with the spherical bubble rise model. Also, simulation results are more coherent than the experiment which shows much larger differences between different runs.

As the bubble diameter in the EPRI test case was prescribed arbitrarily, a parametric study of cases with the smallest prescribed inlet was performed, by varying the bubble diameter from 0.75 cm to 1.25 cm in 0.05 cm steps and using the pure (no added multiplication factor) Schiller-Naumann drag model. As shown in Fig. 16, no large variation of DF was obtained in the vicinity of the value 1.00 cm, or towards smaller diameters. Large variations of DF were observed only when the diameter was increased by 20% or more. The increase of the calculated DF with the increase of bubble diameter was not expected at first, since it was assumed that in bigger bubbles particles take longer to reach the bubble surface. However, since the rise velocity of bigger bubbles is also higher, it leads to a higher relative velocity between bubbles and liquid, increasing the gas circulation velocity in bubbles, which in turn increases the overall DF. Thus, in the proposed model, the effect of the increased bubble diameter on the increase of the rise velocity dominates.

The results of same runs as in Fig. 15 but with the Schiller-Naumann drag model multiplied with  $K_{CD} = 0.5$  show that a better agreement with

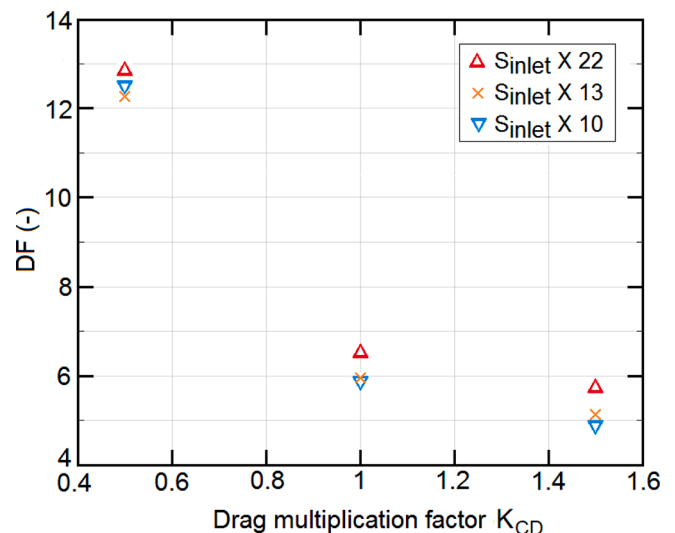


Fig. 14. EPRI experiments: decontamination factor for different inlet areas with various drag multiplication factors  $K_{CD}$ .

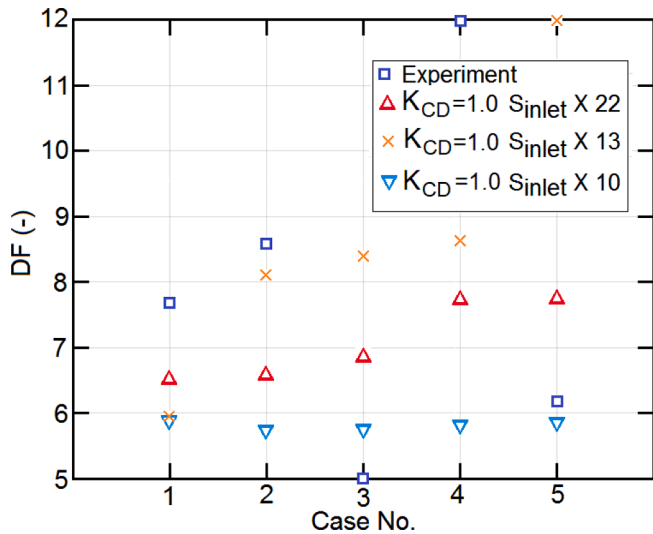


Fig. 15. EPRI experiments: experimental and calculated decontamination factors (default Schiller-Naumann drag model).

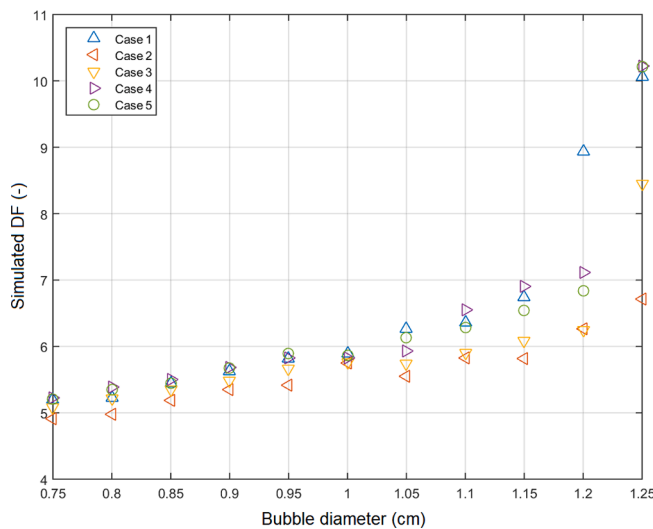


Fig. 16. EPRI experiments: experimental and calculated decontamination factors (default Schiller-Naumann drag model) with variation of bubble diameter and smallest inlet.

experimental values are achieved without the multiplication (see Fig. 16). This is probably due to the quite low air and particle velocities at the inlet (because of the wider inlet area) which is in accordance with the results from the LINX experiment. The result that is in best agreement with experiment is the E4 case where the experimental decontamination factor is the highest.

The comparison of the results from both sets of simulations (with and without the drag model multiplication factor) are presented in Fig. 17 (simulation vs. experimental decontamination factor). The bold line represents a hypothetical perfect agreement between experiment and simulation. As already stated, the results with best agreement with the experiment are the cases with the original Schiller-Naumann drag correlation. For cases with highest experimental decontamination factor (e.g. case E4), the best results are achieved with narrowest inlet and with the drag multiplication by  $K_{CD} = 0.5$ .

Considering both simulated sets of experiments (SCRUPOS and EPRI), although simulation decontamination factors sometimes differ significantly from experimental ones, values are still of the same order of magnitude, which may be considered a promising result, given the

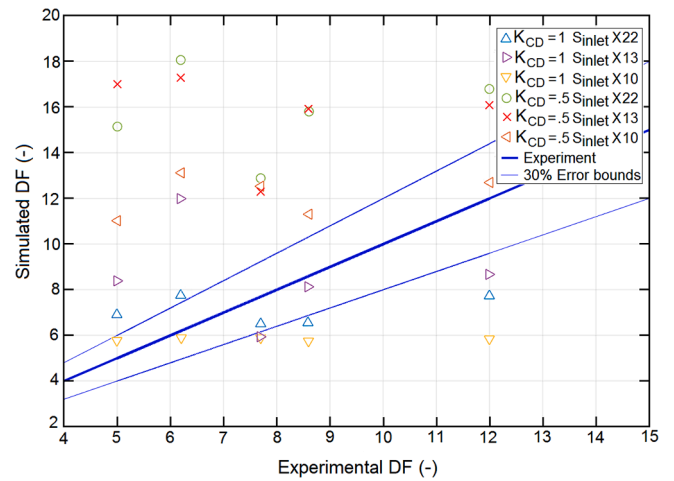


Fig. 17. EPRI experiments: overall comparison of experimental and calculated decontamination factors.

complexity of the process due to the many interacting phenomena, and the necessary simplifying assumptions necessary for the theoretical treatment. In addition, most simulations of pool scrubbing up to now were performed with lumped-parameter codes, which describe phenomena on a much higher length scale than multi-fluid description.

### 5. Conclusions

A model of pool scrubbing rise region, based on multi-fluid modelling considering four phases (liquid, gas, and two particle phases – within liquid and within gas), is proposed, with implementation of the following features:

- a particle drag force from the literature, modified with a multiplication factor;
- a model of particle transport from gas to liquid phase, based on simulations of particle motion within rising spherical bubbles.

The agreement between two sets of experimental and simulation results of a bubble swarm in a quiescent liquid was found to be satisfactory in general. This validation was performed to minimise the possibility of compensating errors.

Simulations of pool scrubbing, at the conditions of two different experiments, were performed. The calculated decontamination factors were of the same order of magnitude as the ones determined experimentally. This shows that the proposed modelling, which is one of the few using local instantaneous description so far, captures the governing mechanisms of pool scrubbing.

#### CRediT authorship contribution statement

**Matic Kunšek:** Conceptualization, Methodology, Validation, Writing – original draft. **Leon Cizelj:** Writing – review & editing, Supervision, Project administration. **Ivo Kljenak:** Conceptualization, Writing - final draft, Supervision.

#### Declaration of Competing Interest

The authors declare that they have no known competing financial interests or personal relationships that could have appeared to influence the work reported in this paper.

#### Acknowledgment

The authors acknowledge the financial support from the Slovenian

Research Agency through research grant P2-0026 and Young researcher grant for Matic Kunšek.

## References

- Abe, Y., Fujiwara, K., Saito, S., Yuasa, T., Kaneko, A., 2018. Bubble dynamics with aerosol during pool scrubbing. *Nucl. Engng Des.* 337, 96–107.
- Ansari, M.R., Nimvari, M.E., 2011. Bubble viscosity effect on internal circulation within the bubble rising due to buoyancy using the level set method. *Annals Nucl. Energy* 38, 2770–2778.
- Besagni, G., Guédon, G.R., Inzoli, F., 2018. Computational fluid-dynamic modeling of the mono-dispersed homogeneous flow regime in bubble columns. *Nucl. Engng Des.* 331, 222–237.
- Bonart, H., 2012. Implementation and validation of a solver for direct numerical simulations of turbulent reacting flows in OpenFoam. B.Sc. Thesis, Karlsruhe Institute of Technology, Germany.
- Dehbi, A., Suckow, D., Guentay, S., 2001. Aerosol retention in low-subcooling pools under realistic accident conditions. *Nucl. Engng Des.* 203, 229–241.
- Dehbi, A., Suckow, D., Lind, T., Guentay, S., Danner, S., Mukin, R., 2016. Key findings from the Artist project on aerosol retention in a dry steam generator. *Nucl. Eng. Technol.* 48, 870–880.
- Dhotre, M.T., Smith, B.L., 2007. CFD simulation of large-scale bubble plumes: Comparisons against experiments. *Chem. Engng Sc.* 62, 6615–6630.
- Escudero Berzal, M., Marcos Crespo, M.J., Swiderska-Kowalczyk, M., Martin Espigares, M., Lopez-Jimenez, J., 1995. State-of-the-Art Review on Fission Product Aerosol Pool Scrubbing under Severe Accident Conditions, Report EUR 16241, European Commission, p. 50.
- Frank, T., Shi, J., Burns, A.D., 2004. Validation of Eulerian multiphase flow models for nuclear safety application, 3rd Int. Symp. on Two-Phase Flow Modelling and Experimentation.
- Fujiwara, K., Kikuchi, W., Nakamura, Y., Yuasa, T., Saito, S., Kaneko, A., Abe, Y., 2019. Experimental study of single-bubble behavior containing aerosol during pool scrubbing. *Nucl. Engng Des.* 348, 159–168.
- Garner, F.H., Hammerton, D., 1954. Circulation inside gas bubbles. *Chem. Engng. Sc.* 3, 1–11.
- Ghiaasiaan, S.M., Yao, G.F., 1997. A theoretical model for deposition of aerosols in rising spherical bubbles due to diffusion, convection, and inertia. *Aerosol Sc. and Technol.* 26 (2), 141–153.
- Greenshields, C.J., 2015. OpenFoam User Guide, version 3.0.1. OpenFOAM Foundation Ltd.
- Herranz, L.E., Fontanet, J., 2013. Analysis of the effect of water ponds on HTR confinement behavior under accident conditions. *Prog. Nucl. Energy* 67, 7–14.
- Hinds, W.C., 1999. *Aerosol Technology – Properties, Behavior and Measurement of Airborne Particles*, 2nd ed., John Wiley & Sons.
- Hozumi, Y., Yoshizawa, Y., 1992. Numerical analysis of dust particles motion inside gas bubbles for flue gas desulfurization in a jet bubbling reactor. *Comput. Fluids* 21, 211–219.
- Kuhlman, M.R., Gieseke, J.A., Merilo, M., Oehlberg, R., 1986. Scrubbing of fission product aerosols in LWR water pools under severe accident conditions. Proc. Symp. Source Term Evaluation for Accident Conditions, Columbus, OH, USA, 28 October – 1 November 1985.
- Kunšek, M., Saito, Y., Ito, D., 2016. Experiments on bubbly to slug flow transition in a vertical cylindrical tube. Int. Conf. “Nuclear Energy for New Europe 2016”, Portoroz, Slovenia.
- MATLAB®, 2018. Curve Fitting Toolbox, version 7.10.0 (R2018a). The MathWorks, Inc.
- OECD/Nuclear Energy Agency 1999. OECD/CSNI Specialist Meeting on Nuclear Aerosols in Reactor Safety - Summary and Conclusions. NEA/CSNI/R(99)5.
- Ozaki, T., Hibiki, T., Miwa, S., Mori, M., 2018. Code performance with improved two-group interfacial area concentration correlation for one-dimensional forced convective two-phase flow simulation. *J. Nucl. Sc. Technol.* 55 (8), 911–930.
- Powers, D.A., 1997. A Simplified Model of Decontamination by BWR Steam Suppression Pools. NUREG/CR-6153, SAND93-2588, Sandia National Laboratories, Albuquerque, USA.
- Ramsdale, S.A., Bamford, G.J., Fishwick, S., Starkie, H.C., 1992. Status of Research and Modelling of Water-Pool Scrubbing. Report EUR 14566, Commission of the European Communities.
- Rzehak, R., Krauß, M., Kováts, P., Zähringer, K., 2017. Fluid dynamics in a bubble column: New experiments and simulations. *Int. J. Multiphase Flow* 89, 299–312.
- Selma, B., Bannari, R., Proulx, P., 2010. A full integration of a dispersion and interface closures in the standard k-ε model of turbulence. *Chem. Engng Sc.* 65, 5417–5428.
- Simiano, M., 2005. Experimental Investigation of Large-Scale Three Dimensional Bubble Plume Dynamics. Diss. ETH No. 16220, Swiss Federal Institute of Technology Zurich, Switzerland.
- Taitel, Y., Bornea, D., Dukler, A., 1980. Modelling flow pattern transitions for steady upward gas-liquid flow in vertical tubes. *AIChE J.* 26, 345–354.
- Turni, M., 2016. Experimental Study and Modeling of a Pool Scrubbing System for Aerosol Removal. Tesi di Laurea, Politecnico di Milano, Italy.
- Wardle, K.E., Weller, H.G., 2013. Hybrid multiphase CFD solver for coupled dispersed/segregated flows in liquid-liquid extraction. *Int. J. Chem. Engng* 2013. Article ID 128936, 1–13.
- Wassel, A.T., Mills, A.F., Bugby, D.C., Oehlberg, R.N., 1985. Analysis of radionuclide retention in water pools. *Nucl. Engng Design* 90, 87–104.